

## Light ion emission from reactions induced by 0.8–2.4 GeV $^{16}\text{O}$ projectiles

R. L. Auble, J. B. Ball, F. E. Bertrand, C. B. Fulmer, D. C. Hensley, I. Y. Lee, R. L. Robinson,  
P. H. Stelson, and C. Y. Wong

*Oak Ridge National Laboratory, Oak Ridge, Tennessee 37830*

D. L. Hendrie

*Lawrence Berkeley Laboratory, Berkeley, California 94720*

H. D. Holmgren and J. D. Silk

*University of Maryland, College Park, Maryland 20742*

(Received 8 June 1983)

Differential cross sections for the production of  $Z=1, 2$  particles are measured for 52, 100, and 147 MeV/nucleon  $^{16}\text{O}$  projectiles. The projectile energy and target-mass dependencies are examined and compared with measurements in other projectile energy regimes. Central and peripheral collisions are found to give comparable contributions to the light ion yields, with the dominant process varying with the emission angle. The spectra are parametrized both in terms of a single heated, moving source and as a sum of fragmentation and central collision sources, and velocity and temperature parameters are presented. For composite particles, coalescence parameters and source radii are also extracted.

[NUCLEAR REACTIONS Ni( $^{16}\text{O},X$ ),  $E=0.8, 1.6, 2.4$  GeV; Au( $^{16}\text{O},X$ ),  $E=1.6, 2.4$ , GeV; Al, Sn( $^{16}\text{O},X$ ),  $E=1.6$  GeV; measured  $\sigma(E,\theta)$  for  $X=p, d, t, ^3\text{He}, ^4\text{He}$ ; deduced model parameters.]

### I. INTRODUCTION

Large cross sections have been reported for the emission of high energy light particles from heavy ion induced reactions using a variety of projectile masses and energies. In this paper we report measurements of yields of  $Z=1,2$  particles from reactions of 52, 100, and 147 MeV/nucleon  $^{16}\text{O}$  ions and a variety of targets. Most of the previously reported measurements have concentrated on the projectile energy regions  $\leq 20$  MeV/nucleon (Refs. 1–5) or  $\geq 300$  MeV/nucleon (Refs. 6 and 7), and only limited data have been reported at medium projectile energies.<sup>8–10</sup> Since the systematics of inclusive spectra are possible indicators of changes in the dominant reaction mechanisms, the present studies were made to add to our knowledge of these processes at intermediate projectile energies.

The comparison of data obtained under differing experimental conditions can be made in several ways. Model independent comparisons are difficult owing to the differences in spectral shapes at different bombarding energies and are limited to gross features such as integral cross sections. Alternatively, the data can be fit with various models and the parameters extracted from the fits can be examined as a function of a given experimental quantity, such as the projectile energy, to look for discontinuities which may signal a change in the reaction process. One such parametrization is in terms of emission by a heated moving source.<sup>4</sup> Velocity and temperature parameters are extracted from fits to the present data and compared with those reported at other projectile energies. Another model, which can be applied to composite particle ( $^2\text{H}, ^3\text{H}, \dots$ ) spectra, is the coalescence model<sup>11</sup> in which the spectrum of a particle of mass  $A$  is related to the  $A$ th

power of the nucleon spectrum. The coalescence radii are extracted and compared with values reported at other projectile energies.

The moving source and coalescence models are found to be limited in their ability to fit all of the data at the projectile energies used in these studies. A model which includes both peripheral and central collision components, with independent longitudinal and transverse momentum widths, is found to provide good fits to most of the light ion spectra.

### II. EXPERIMENTAL DETAILS

The measurements were made on the low energy beam line at the LBL Bevalac. Tune-up beams of 100 MeV/nucleon  $^2\text{H}$  and  $^4\text{He}$  were used to obtain detector energy calibrations prior to making measurements with  $^{16}\text{O}$  projectiles. The energies of the various beams were determined from the magnetic field setting of a beam analyzing magnet located before the scattering chamber. The effective radius of curvature of this magnet was determined by placing detectors into the  $^4\text{He}$  beam and using various absorbers to determine the beam energy. A value of 2.2350 m, obtained at a field setting of 1.323 T, was used for all other projectile energy determinations. No data were available concerning possible changes in the effective radius at different field settings, and it was assumed to be constant.

The number of incident projectiles was measured by integrating the current from an ion chamber located on the beam axis approximately 2 m beyond the target position. This chamber was calibrated at each projectile energy by placing a thin plastic scintillator in front of the chamber

and counting the number of incident projectiles. This technique could be applied up to beam intensities of  $\approx 4 \times 10^5$  particles/spill before the scintillator began to saturate. At higher intensities, the chamber was calibrated against the number of projectiles scattered into plastic scintillators located off the beam axis. The uncertainty in the ion chamber calibration, based on the spread in values obtained at several different beam intensities, is estimated to be  $\pm 8\%$ .

Eight detector telescopes were used in these measurements, each consisting of a 1 mm thick silicon surface barrier  $\Delta E$  detector and a 12.7 cm long NaI(Tl)  $E$  detector. Four detectors were located outside the scattering chamber, approximately 2 m from the target, at angles of 6, 12, 18, and 24 deg and subtended solid angles of 0.34–0.37 msr as defined by 3.8 cm i.d.  $\times$  2.54 cm thick Pb collimators. These telescopes were separated from the vacuum chamber by a 0.013 cm thick Mylar window and an  $\approx 3$  cm air gap, and the NaI detectors were covered by a 0.0076 cm thick aluminum window. The four remaining telescopes were located inside the scattering chamber at 45, 85, 115, and 155 deg at a distance of  $\approx 20$  cm from the target and used 1.59 cm i.d.  $\times$  2.54 cm thick Cu collimators to give solid angles of 4.8–5.6 msr. The NaI detectors used at these angles had entrance windows of 0.025 cm aluminum. The light ion energies accepted by these detectors were limited on the low energy end by absorption in the  $\Delta E$  detector and windows, and on the high energy end by the range of the particles. The energies which could be detected with these telescopes were approximately 14–210 MeV ( $^1\text{H}$ ), 19–280 MeV ( $^2\text{H}$ ), 22–330 MeV ( $^3\text{H}$ ), 49–740 MeV ( $^3\text{He}$ ), and 55–840 MeV ( $^4\text{He}$ ). However, in many cases the spectra were distorted at the lowest energies due to straggling in the  $\Delta E$  detector and various windows, and in most of the data analyses low energy cutoffs approximately 5 MeV higher than the values listed were applied.

The energy calibrations were determined by placing each detector into low intensity 100 MeV/nucleon  $^2\text{H}$  and  $^4\text{He}$  beams. Suitable absorbers placed in front of the detectors provided several calibration points for each projectile. The uncertainty in the energy calibration is estimated to be  $\pm 1.5\%$  except at the lowest measured energies, where window corrections become important. Corrections for detector efficiency for  $^2\text{H}$  and  $^4\text{He}$  were also obtained in these measurements by determining the peak/tail ratios from the  $E$  vs  $\Delta E$  spectra. Published reaction losses for protons<sup>12</sup> and the present data for alpha particles indicate that the efficiency (peak/total) can be expressed to a good approximation by  $\epsilon = 1 - kE^{1.45}$ , where  $E$  is the particle energy in MeV and  $k$  depends on the  $Z$  and  $A$  of the detected particle. The data for deuterons were restricted to a narrow range of energies, so no functional dependence could be obtained. We have assumed that this same expression holds for  $A=2,3$  particles. The values of  $k$  for  $^3\text{H}$  and  $^3\text{He}$  were estimated by assuming that the total reaction cross section is the same as that for  $^4\text{He}$  and correcting for the particle range. The measured losses and values of  $k$  used in these studies are summarized in Table I.

Table II summarizes the projectile-target combinations

TABLE I. Measured losses due to nonelastic reactions in 12.7 cm long NaI(Tl) detectors and deduced efficiency correction factors. The detection efficiency is given by  $\epsilon = 1 - kE^{1.45}$ , where  $E$  is the particle energy in MeV.

Particle	Measured losses		Efficiency correction factors	
	$E$ (MeV)	tail/total (%)	Particle	$10^4 \times k$
$^2\text{H}$	185	26	$^1\text{H}$	1.18
	200	29.3	$^2\text{H}$	1.36
$^4\text{He}$	50	0.6	$^3\text{H}$	1.06
	100	1.9	$^3\text{He}$	0.309
	200	5.5	$^4\text{He}$	0.253
	400	15.2		

used in these measurements. The targets were rolled foils (natural abundance) 5 cm in diameter, with thicknesses determined by weighing, of 26 (Al), 43 (Ni), 57 (Sn), and 55 (Au) mg/cm<sup>2</sup>. Assuming that the targets have uniform areal density, the uncertainty in the target thickness is estimated to be  $\pm 2\%$ . Background measurements were made by using a blank target frame. It was found that at 6° the deuteron spectra, and to a lesser degree the proton and triton spectra, contained a low energy background component of undetermined origin. This placed lower limits of 100–150 MeV on the usable 6° data for these particles.

### III. RESULTS

Proton spectra resulting from the bombardment of Sn with 100 MeV/nucleon  $^{16}\text{O}$  projectiles are displayed in Fig. 1. At small angles, the cross sections are observed to peak at energies close to  $E/A$  of the projectile, suggesting peripheral fragmentation as the source of these particles. As the emission angle increases, the fragmentation component decreases in intensity, the spectra acquire an approximately exponential energy dependence characteristic of thermal emission, and the angular distribution becomes more isotropic. Momentum plots of the 6° proton spectra, measured for the Ni target at the three different projectile energies, are shown in Fig. 2. The solid lines are fits to

TABLE II. Summary of  $^{16}\text{O}$  projectile energy-target combinations and beam fluences used in the present studies.

$E/A_{\text{proj}}$ (MeV)	Target	$Q$ ( $e\mu\text{C}$ ) ( $\pm 8\%$ )
51.8	Ni	0.0411
100.1	Al	0.0181
100.1	Ni	0.0873
100.1	Sn	0.0451
100.1	Au	0.0575
147.0	Ni	0.0478
147.0	Au	0.0714

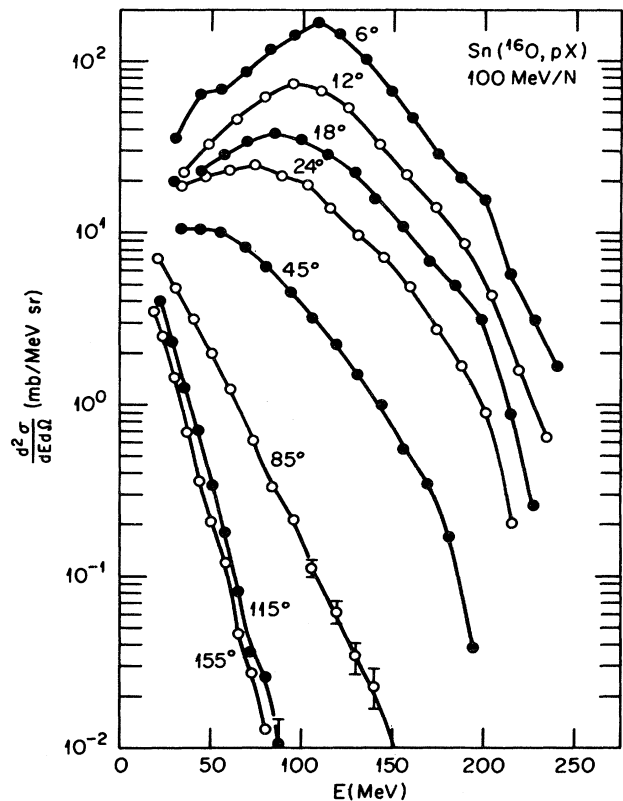


FIG. 1. Proton energy spectra from 1.6 GeV  $^{16}\text{O}$  on a Sn target. For  $E > 200$  MeV, the spectra are distorted due to the finite length of the detector. The error bars are due solely to counting statistics. The lines are drawn to guide the eye.

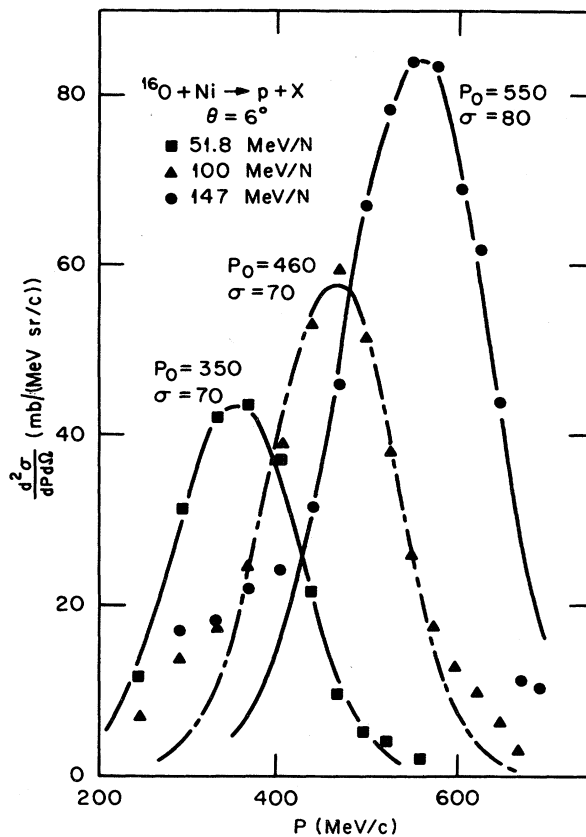


FIG. 2. Momentum distributions of protons from  $^{16}\text{O} + \text{Ni}$  reactions. The curves are Gaussian distributions with means ( $P_0$ ) and widths ( $\sigma$ ) as indicated.

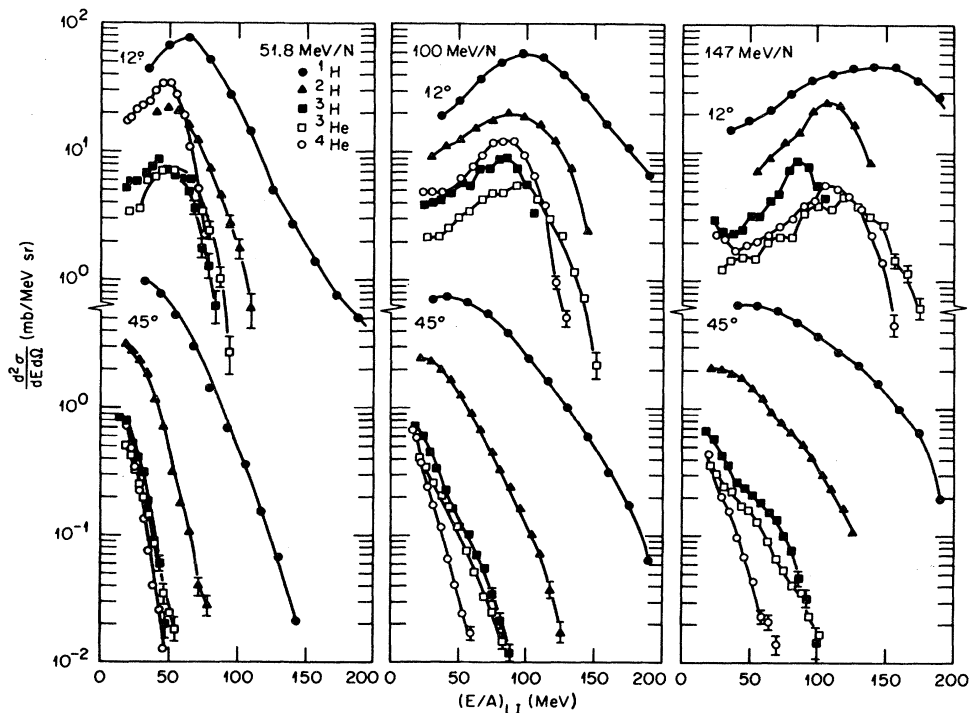


FIG. 3. Differential cross sections for light ions emitted at  $12^\circ$  and  $45^\circ$  in  $\text{Ni} + ^{16}\text{O}$  collisions at projectile energies at 51.8, 100, and 147 MeV/nucleon. The cross sections are plotted versus  $E/A$  of the light ion.

TABLE III. Measured yields of light particles from 51.8, 100, and 147 MeV/nucleon  $^{16}\text{O}$  reactions. The lower limits on the energy integrations are approximately 15 MeV ( $^1\text{H}$ ), 21 MeV ( $^2\text{H}$ ), 24 MeV ( $^3\text{H}$ ), 52 MeV ( $^3\text{He}$ ), and 60 MeV ( $^4\text{He}$ ). The uncertainties introduced by the angular extrapolations are given.

$(E/A)_{\text{proj}}$ (MeV)	Target	$\sigma$ (b)				
		$^1\text{H}$	$^2\text{H}$	$^3\text{H}$	$^3\text{He}$	$^4\text{He}$
51.8	Ni	4.17±0.09	1.91±0.06	0.80±0.02	0.63±0.02	2.9±0.2
100	Al	3.31±0.07	1.57±0.06	0.59±0.02	0.56±0.04	1.7±0.3
	Ni	4.62±0.10	2.04±0.06	0.87±0.03	0.71±0.04	2.0±0.2
	Sn	6.47±0.15	3.30±0.07	1.56±0.03	0.86±0.04	2.5±0.3
	Au	7.9±0.02	3.98±0.09	1.89±0.03	0.96±0.10	2.8±0.3
147	Ni	5.5±0.02	2.23±0.06	0.86±0.04	0.75±0.06	1.8±0.4
	Au	8.2±0.03	3.91±0.15	1.75±0.08	0.90±0.12	2.4±0.5

the data assuming momentum distributions of the form

$$\exp[-(p-p_0)^2/2\sigma^2],$$

with the values of  $p_0$  and  $\sigma$  given in the figure, and the data are seen to be reproduced quite well except at the lowest momenta. The mean momenta ( $p_0$ ) are found to be approximately equal to the momenta corresponding to the projectile velocity and  $\sigma$  is found to have only a weak dependence on the projectile energy. From similar plots for the other detected particles, it is found that the width for particles of mass  $A$  is given to a good approximation by

$$\sigma_A^2 = \sigma_0^2 A (A_p - A) / (A_p - 1),$$

where  $A_p$  is the projectile mass. This result is expected for collisions in which the momentum transfer is small compared to  $\sigma_0$ .<sup>13</sup> The values of  $\sigma_0$  deduced from the present small angle proton spectra, 70–80 MeV/c, are found to be somewhat smaller than the value 85.1 MeV/c reported for 43 MeV/nucleon  $^{20}\text{Ne}$  projectiles.<sup>9</sup> As noted in Ref. 13, if the fragmentation is assumed to occur early in the collision, then  $\sigma_0$  can be related to the Fermi momentum  $p_F$  of the nucleons in the projectile through the relation  $\sigma_0^2 = p_F^2/5$ . Alternatively, if one assumes that emission occurs after thermal equilibrium is attained, the width can be related to the temperature by

$$T = \frac{A_p}{A(A_p - A)} \frac{\sigma_A^2}{m_N}$$

where  $m_N$  is the nucleon mass.<sup>13</sup> The present small angle measurements give temperatures in the range 5–7 MeV,

or  $p_F = 160$ – $190$  MeV/c. A possible explanation for the small value for  $p_F$  is discussed in Sec. IV.

Differential cross sections for various  $Z=1,2$  particles emitted in  $^{16}\text{O} + \text{Ni}$  collisions, plotted versus  $E/A$  of the particle, are compared in Fig. 3. For all particles and all three projectile energies, the general characteristics of the spectra are as noted above for protons. There are several interesting points to be seen in these spectra. For example, at the lower projectile energy the small angle proton spectra peak at energies greater than  $E/A$  of the projectile. Also, the beam energy dependence is not the same for the various particles. For example, note the rapid decrease in cross section for alpha particle emission and the increasing disparity between  $^3\text{H}$  and  $^3\text{He}$  spectral shapes with increasing projectile energy.

In Table III, the integrated cross sections are given for particles having energies above the detector thresholds. The extrapolations to  $0^\circ$  and  $180^\circ$  were guided by the requirement that  $d\sigma/d\theta=0$  at these angles. Most of the uncertainty introduced by the angular extrapolations is from the  $0^\circ$ – $6^\circ$  interval, and estimates are given in Table III. In order to obtain integral cross sections, the energy spectra were extrapolated to  $E=0$  by assuming that the invariant cross section,

$$\frac{1}{p} \frac{d^2\sigma}{dE d\Omega},$$

is approximately constant and isotropic as  $p \rightarrow 0$ . Values determined in this way are given in Table IV. Comparison of Tables III and IV shows that the contribution from the low energy region can be quite substantial, particularly for  $Z=2$  particles. However, comparison of

TABLE IV. Integral cross sections obtained by extrapolation of the measured spectra over all energies and angles. Uncertainties are estimated to be  $\pm 15\%$ .

$E/A$ (proj)	Target	$\sigma$ (b)				
		$^1\text{H}$	$^2\text{H}$	$^3\text{H}$	$^3\text{He}$	$^4\text{He}$
51.8	Ni	5.83	2.69	1.19	1.27	5.5
100	Al	3.92	1.96	0.85	0.74	2.4
	Ni	5.72	2.79	1.15	1.05	3.3
	Sn	8.20	4.59	2.28	1.33	5.2
	Au	10.2	5.75	3.08	1.55	6.6
147	Ni	6.71	2.78	1.11	1.03	2.8
	Au	10.6	4.85	2.48	1.30	4.9

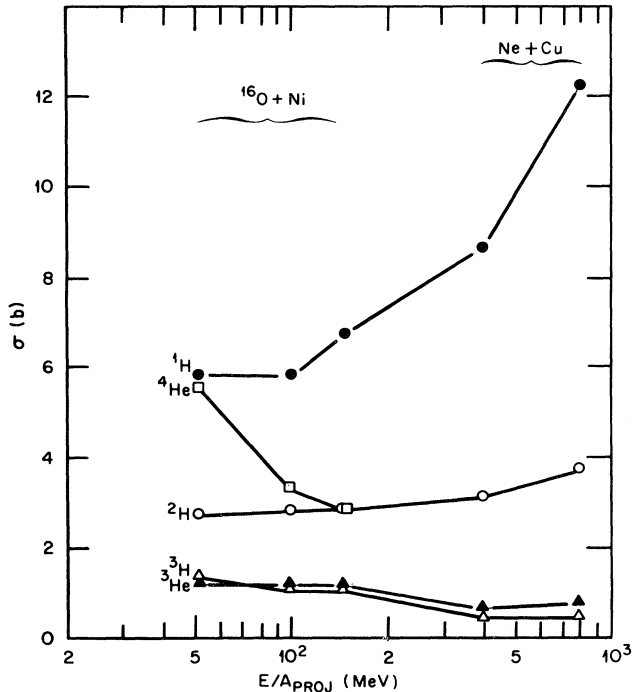


FIG. 4. Integral cross sections for  $Z=1,2$  particles from  $^{16}\text{O} + \text{Ni}$  (the present studies) and  $\text{Ne} + \text{Cu}$  (Ref. 7) reactions.

values obtained for several different choices of shapes for the low energy spectra leads to the conclusion that the error in the extrapolated portion of the integral cross section is not more than  $\pm 25\%$ . This would contribute an uncertainty of  $\pm 10\text{--}15\%$  in the integral cross sections. These values are plotted in Fig. 4 and are compared with cross sections reported<sup>7</sup> for 400 and 800 MeV/nucleon Ne on Cu. While the proton and deuteron yields are found to increase with increasing projectile energy, the yields of  $A=3$  and 4 fragments decrease. This general behavior has been noted previously and reproduced in part by a fireball calculation.<sup>10</sup>

The target mass dependence of light ion emission was examined at 100 MeV/nucleon projectile energy. These results have been reported previously<sup>14</sup> but are included here for completeness. The proton differential cross sections, integrated over proton energies above the detector lower limit, are plotted in Fig. 5. At small angles, the cross sections are observed to increase approximately as  $A_{\text{target}}^{1/3}$ . This is consistent with the behavior one would expect for reactions occurring on the periphery of the target nucleus. Thus, "peripheral fragmentation" appears to dominate at small emission angles. As the angle is increased, the target mass dependence approaches  $A_{\text{target}}^{2/3}$ , suggesting that central collisions become dominant at angles greater than about 45 deg.

The integral cross sections for the various detected particles, from Table III, are plotted in Fig. 6. Since these values are dominated by the smaller angles, an approximately  $A_{\text{target}}^{1/3}$  dependence is obtained for all particles. However, the deuteron and triton yields are observed to

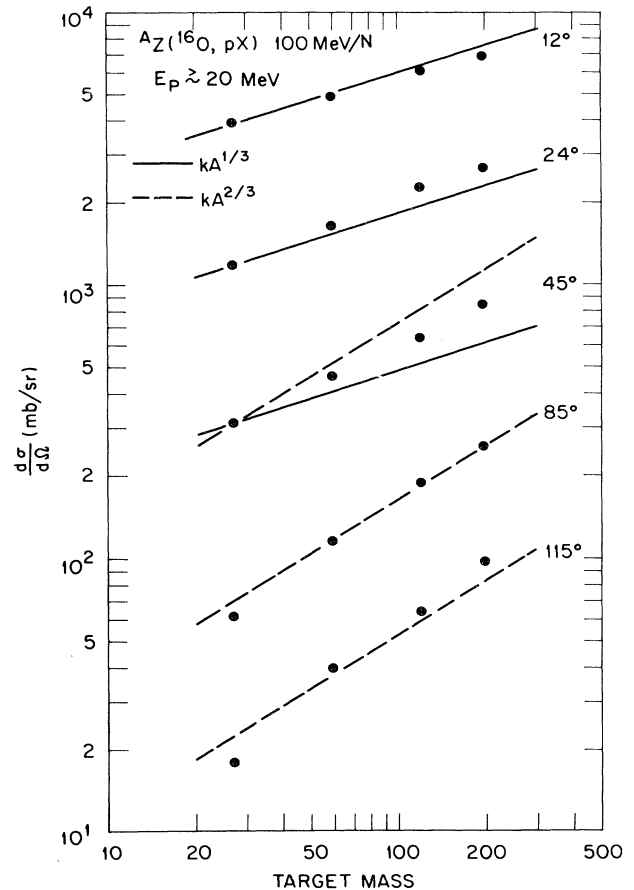


FIG. 5. Differential cross sections for emission of protons with energies  $\geq 20$  MeV at various laboratory angles, plotted as a function of the target mass. The solid and dashed lines show the slopes expected for  $A^{1/3}$  and  $A^{2/3}$  target mass dependences, respectively.

increase more rapidly between Ni and Sn. Such a dependence on  $N/Z$  of the target is consistent with predictions of the coalescence model discussed in Sec. IV. Proton integral cross sections, from Table IV, are plotted in Fig. 7 and compared with those obtained using 400-, 800-, and 2100-MeV/nucleon Ne projectiles.<sup>7</sup> The target mass dependence is observed to change with increasing projectile energy and suggests that central collisions and nucleon-nucleon interactions may dominate at higher projectile energies.

#### IV. DATA ANALYSIS

##### A. Single thermal source

As a first step in analyses of these results, and to provide a common basis for comparison with measurements at other projectile energies, we attempt to describe the light ion spectra in terms of thermal emission from a heated moving source. The expressions and fitting procedures are identical to those used at lower projectile energies.<sup>5</sup> The "source" is described by temperature ( $T$ ) and

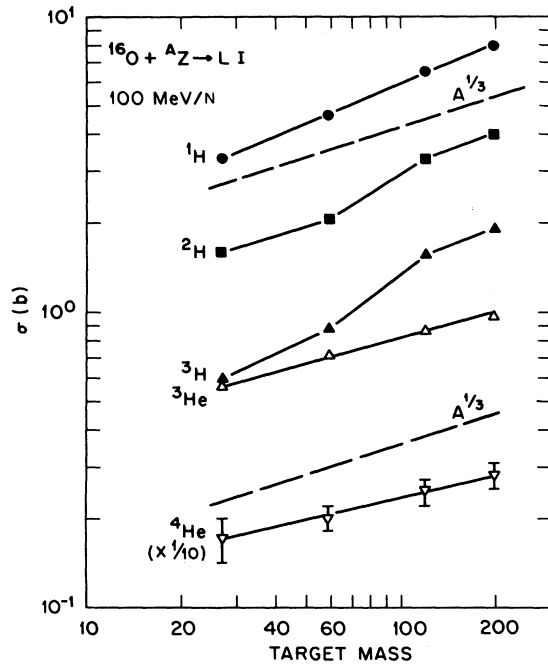


FIG. 6. Light ion emission cross sections, integrated over angle and energies above the detector thresholds, for  $Z=1,2$  particles from 100 MeV/nucleon  $^{16}\text{O}$  on various targets. The dashed lines show the slope for an  $A^{1/3}$  target mass dependence for comparison.

velocity, relative to the projectile velocity, ( $V_s/V_{\text{proj}}$ ) obtained by fitting the data with the expression

$$\frac{d^2\sigma}{d\Omega dE} = K\sqrt{E_L E_R} \exp(-E_R/T), \quad (1)$$

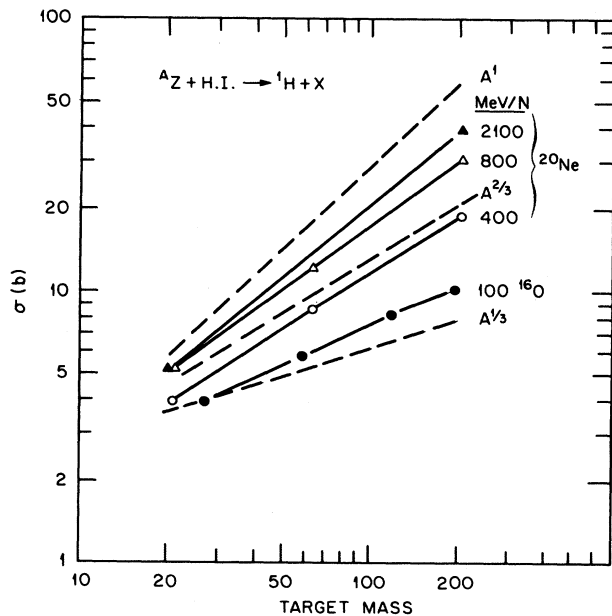


FIG. 7. Integral cross sections for protons from  $^{16}\text{O}$  (the present studies) and  $^{20}\text{Ne}$  (Ref. 7) on various targets. Dashed lines show the slopes expected for various target mass dependences.

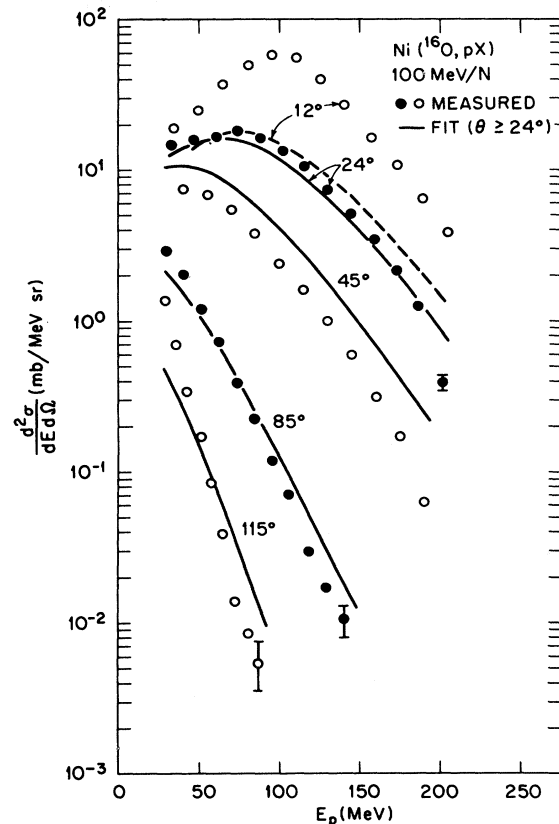


FIG. 8. Fits to proton spectra using a heated moving source. The dashed curve is the  $12^\circ$  spectrum calculated using parameters obtained from fitting the data at  $\theta \geq 24^\circ$ .

where  $E_L$  and  $E_R$  are the particle energies in the laboratory and source rest frames, respectively. Since the data suggest that peripheral fragmentation dominates the small angle spectra, the present fits were restricted to angles  $\geq 24^\circ$ . In Fig. 8, fits are shown for proton spectra mea-

TABLE V. Projectile energy dependence of heated moving source parameters from fitting  $^{16}\text{O} + \text{Ni}$  data.

$(E/A)_{\text{proj}}$	Detected	$V_s/V_{\text{proj}}$	$T$ (MeV)	$K$
51.8 MeV/nucleon	$^1\text{H}$	0.60	11.1	3.4
	$^2\text{H}$	0.58	14.8	0.72
	$^3\text{H}$	0.63	13.8	0.30
	$^3\text{He}$	0.68	15.4	0.16
	$^4\text{He}$	0.66	14.8	0.80
100 MeV/nucleon	$^1\text{H}$	0.54	17.2	1.25
	$^2\text{H}$	0.50	22.6	0.33
	$^3\text{H}$	0.52	21.4	0.12
	$^3\text{He}$	0.56	25.2	0.053
	$^4\text{He}$	0.48	21.9	0.13
147 MeV/nucleon	$^1\text{H}$	0.51	22.0	0.84
	$^2\text{H}$	0.46	28.4	0.22
	$^3\text{H}$	0.47	28.1	0.067
	$^3\text{He}$	0.50	32.3	0.029
	$^4\text{He}$	0.43	31.0	0.048

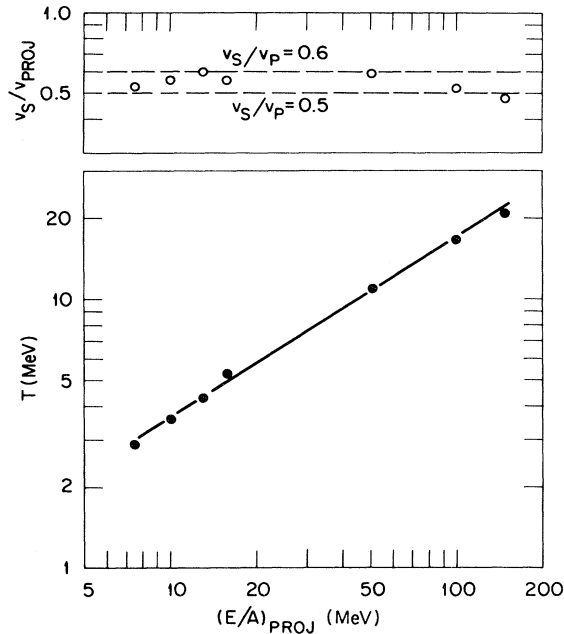


FIG. 9. Velocity and temperature parameters obtained by fitting proton data, from  $^{12}\text{C}$  and  $^{16}\text{O}$  bombardment of Ni at various projectile energies, with a single heated, moving source. The values for  $E/A > 50$  MeV/nucleon are from the present studies, while the lower energy values are from Ref. 5.

sured at 100 MeV/nucleon. The spectral shapes are seen to be reproduced quite well, but the drop in cross section between  $24^\circ$  and  $45^\circ$  is too small. This is probably due to the presence of a fragmentation contribution to the  $24^\circ$

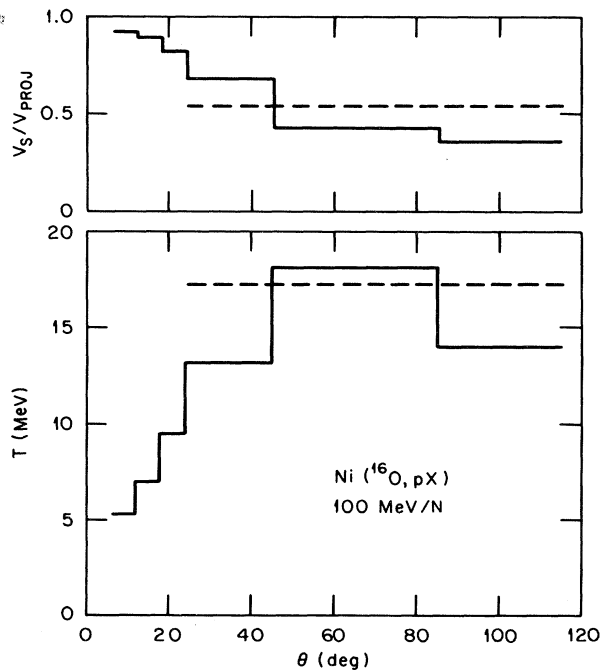


FIG. 10. Moving source velocity and temperature parameters as a function of angle for 100 MeV/nucleon  $^{16}\text{O} + \text{Ni} \rightarrow ^1\text{H} + X$ .

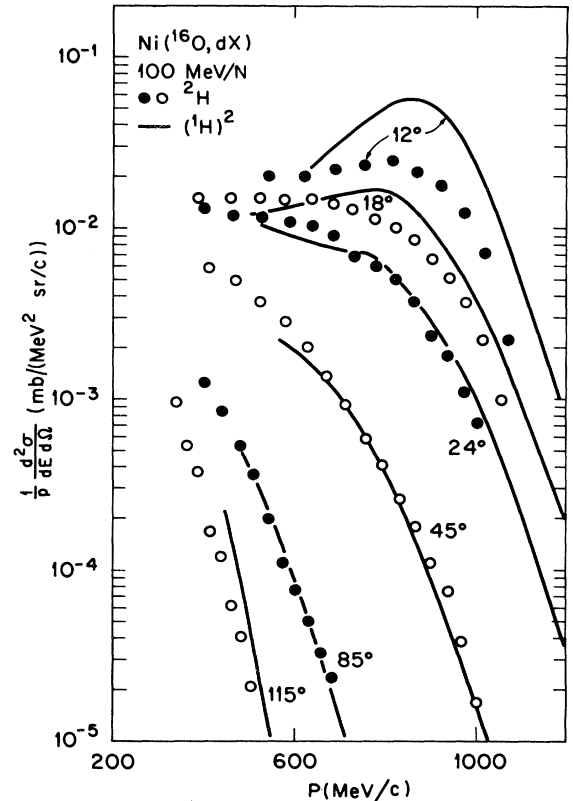


FIG. 11. Comparison of coalescence model predictions with measured deuteron spectra from  $^{16}\text{O} + \text{Ni}$  reactions at 100 MeV/nucleon.

data, but restricting the fits to  $\theta \geq 45^\circ$  was found to cause only minor changes in the "best fit" parameters. Included in Fig. 8 are the measured  $12^\circ$  spectrum and the  $12^\circ$  spectrum calculated using the parameters obtained from fitting the larger angles. Clearly, the rapid increase in cross section at small angles is not consistent with this simple model.

The parameters extracted from fitting the various  $Z=1,2$  particle spectra from  $^{16}\text{O} + \text{Ni}$  are summarized in Table V. In general, the ratio of source to projectile velocities shows little dependence on either fragment mass or projectile energy. However, the temperature increases substantially with increasing projectile energy, and is also somewhat larger for composite particles than for protons. The projectile energy dependence of the velocity and temperature parameters extracted from the proton data can be compared with similar fits made to data obtained in similar studies using lower energy  $^{12}\text{C}$  projectiles.<sup>5</sup> These parameters are plotted in Fig. 9 and are found to have a remarkably smooth behavior for projectile energies from 7.5 to 147 MeV/nucleon. The straight line drawn through the temperature points is given by  $T=0.79(E/A)^{2/3}$  MeV, which is in reasonable agreement with the trend noted<sup>10</sup> for projectile energies up to 800 MeV/nucleon. The target mass dependence is found to be rather weak, the velocity decreasing and the temperature increasing by about 10% in going from aluminum to gold. In order to obtain some feeling for the sensitivity of these parameters to the angu-

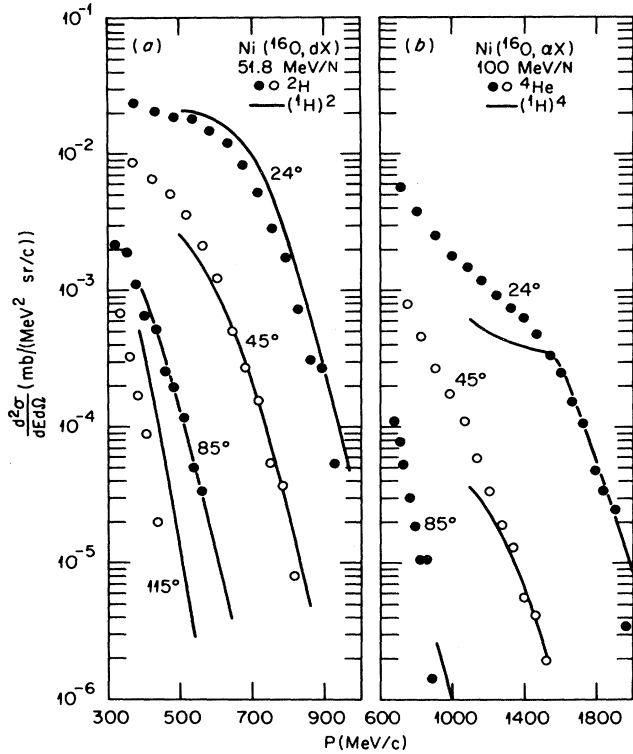


FIG. 12. Coalescence model fits to light particle spectra from  $^{16}\text{O} + \text{Ni}$  reactions. (a) Deuteron spectra at 51.8 MeV/nucleon. (b) Alpha particle spectra at 100 MeV/nucleon.

lar range of the input data, fits were made to pairs of proton spectra at adjacent angles ( $6^\circ$  and  $12^\circ$ ,  $12^\circ$  and  $18^\circ$ , etc.), and the values obtained are shown in Fig. 10. The "average" values for  $\theta \geq 24^\circ$  are included for comparison. It is apparent that the parameters can be strongly influenced by the choice of angles used in the fitting procedure.

### B. Coalescence model

For the case of composite particle emission ( $^2\text{H}$ - $^4\text{He}$ ), one can assume preexisting structures in the projectile, as implied in the discussion above, or a mechanism can be devised in which the composite particles are formed from the appropriate nucleons released in the collision. The

coalescence model<sup>11</sup> has been used to fit the spectra of composite particles emitted in relativistic heavy ion collisions<sup>7</sup> in terms of the measured proton spectra. In this model, the cross section for a particle of mass  $A$  is given by the  $A$ th power of the proton cross section:

$$\left( \frac{1}{p} \frac{d^2\sigma}{dE d\Omega} \right)_A = C_A \left( \frac{1}{p} \frac{d^2\sigma}{dE d\Omega} \right)_{\text{proton}}^A \quad (2)$$

The coalescence parameter  $C_A$  is given by<sup>7,16</sup>

$$C_A = \frac{1}{N!Z!} \left( \frac{4\pi\tilde{P}_0^3}{3m\sigma_T} \right)^{A-1} \frac{A(2S+1)}{2^A} \left( \frac{N_p + N_T}{Z_p + Z_T} \right)^N, \quad (3)$$

where  $N$ ,  $Z$ , and  $A$  refer to the detected particle (of spin  $S$ );  $N_p$  and  $Z_p$  refer to the projectile;  $N_T$  and  $Z_T$  refer to the target nuclei;  $\tilde{P}_0$  is the coalescence radius in momentum space;  $\sigma_T$  is the total reaction cross section; and  $m$  is the nucleon mass. We use the same expression for  $\sigma_T$  as was used in Ref. 7, namely

$$\sigma_T(\text{fm}^2) = \pi(1.29)^2 \{ A_p^{1/3} + A_T^{1/3} - [1 - 0.028 \min(A_p, A_T)] \}^2. \quad (4)$$

The coalescence radius can be further related to the volume ( $V$ ) and radius ( $R$ ) of the emitting source using a thermal model<sup>16,17</sup> in which

$$V = (Z!N!e^{-E_0/kT})^{1/A-1} \frac{3h^3}{4\pi\tilde{P}_0^3} = \frac{4}{3}\pi R^3. \quad (5)$$

As in Ref. 7, the binding energy  $E_0$  is assumed to be much smaller than  $kT$ , so that the radius can be approximated by

$$R = \frac{477}{\tilde{P}_0} (N!Z!)^{1/3(A-1)}. \quad (6)$$

In Fig. 11 we compare the measured deuteron spectra from 100 MeV/nucleon  $^{16}\text{O}$  on Ni with those predicted by the square of the measured proton spectra. The fits are found to be quite good for  $\theta \geq 24^\circ$  but the predicted cross sections are too large at smaller angles, which could imply that protons released in a peripheral collision have less opportunity to interact with other nucleons to form composite particles.

Similar plots were made for other particles and the predicted spectra were normalized to the high energy re-

TABLE VI. Coalescence model parameters for light composite particles emitted in reactions between  $^{16}\text{O}$  and various targets.

$E/A_{\text{proj}}$ (MeV/nucleon)	Target	$^2\text{H}$			$^3\text{H}^a$			$^3\text{He}$			$^4\text{He}^a$		
		$C_A^b$	$\tilde{P}_0$	$R$ (fm)	$C_A^b$	$\tilde{P}_0$	$R$ (fm)	$C_A^b$	$\tilde{P}_0$	$R$ (fm)	$C_A^b$	$\tilde{P}_0$	$R$ (fm)
51.8	Ni	1.7	75	6.4	2	95	4.5	2.5	100	4.3	12	130	3.2
100	Al	5.3	99	4.8	25	131	3.2	16	122	3.5	120	151	2.7
	Ni	3.2	92	5.2	13	129	3.3	7.8	120	3.5	72	158	2.6
	Sn	2.6	90	5.3	6	118	3.6	3.8	115	3.7	17	143	2.8
	Au	2.0	87	5.5	3	111	3.8	2.5	115	3.7	9	142	2.9
147	Ni	4.9	106	4.5	23	142	3.0	12	129	3.3	200	177	2.3
	Au	3.5	104	4.6	13	142	3.0	6.2	133	3.2	60	176	2.3

<sup>a</sup>Values are rough estimates only owing to poor fit.

<sup>b</sup> $C_A$  is from a visual fit of the coalescence model predictions to the measured spectra at  $\theta \geq 24^\circ$ , in units of  $(\text{mb}/\text{MeV}^2 \text{sr})^{1-A}$ .

gions of the measured 24°, 45°, and 85° spectra to extract coalescence parameters. The quality of the fits was somewhat poorer for the lowest projectile energy (51.8 MeV/nucleon) and, also, the model does not work as well at the lower composite particle energies, particularly for alpha particles, where the predicted cross sections are found to be considerably smaller than the measured values. These features are illustrated in Fig. 12 for deuterons at 51.8 MeV/nucleon projectiles and for alpha particles at 100 MeV/nucleon. This is not surprising since other processes, such as emission of preformed composites, are expected to contribute to the low energy part of the spectra. Even though the fits are not as impressive as those reported at higher projectile energies,<sup>7</sup> the  $C_A$ 's extracted from these data are believed to be useable, within a factor of 2, for comparison purposes. The values of  $C_A$ ,  $\bar{P}_0$  and  $R$  are summarized in Table VI, and in Fig. 13 radius parameters  $R$  from the present measurements are compared with those reported in the reactions U(<sup>16</sup>O, fission + LI) (where LI denotes light ion) at 20 MeV/nucleon (Ref. 15) and NaF,Cu,Pb(Ne,LI) at 400, 800, and 2100 MeV/nucleon.<sup>7</sup> The radius of the interaction region is seen to decrease from a value comparable to the sum of the combined target and projectile radii at 20 MeV/nucleon to a value approximately equal to the projectile radius at higher projectile energies. It is also apparent that the values become significantly smaller as the

mass of the emitted particle is increased, although the differences become less pronounced above 400 MeV/nucleon.

### C. Two component model

Both the heated moving source and coalescence models are found to be capable of fitting the experimental data over selected angular and energy regions, and the parameters extracted from these fits may provide some interesting insights into the reaction mechanisms contributing to light ion emission. However, neither model is able to reproduce the present data over the complete range of ejectile emission angles or energies. As noted in Sec. III, the data suggest that the reactions involved can be roughly divided into two categories: (1) fragmentation of the projectile on the periphery of the target nucleus resulting in beam velocity particles concentrated at small angles and (2) central collisions characterized by a source having a velocity about half that of the incident projectiles. A parametrization was employed which includes both components,<sup>18</sup> and the invariant cross section is expressed as a sum of the two contributions,

$$\frac{1}{p} \frac{d^2\sigma}{dE d\Omega} = F_C(\bar{p}) + F_F(\bar{p}), \quad (7)$$

where the subscripts  $C$  and  $F$  indicate the central collision and fragmentation contributions, respectively. Each component is described in terms of a momentum distribution. The momentum distribution of the (projectile) fragmentation component arises from the nucleonic Fermi motion. It is roughly isotropic in the projectile frame and can be adequately described by a Gaussian distribution. On the other hand, the momentum distribution of the central component depends on the initial momentum distribution, the degree of thermalization, and the impact parameter averaging. It need not be isotropic in its source frame and it need not have the shape of a Gaussian distribution. The deviations from isotropy, as indicated by the difference in the longitudinal and transverse momentum distributions, may be a measure of the departure from thermal equilibrium. In our analysis, the non-Gaussian nature of the central component shows up readily in the experimental data, especially in the higher energy collisions. It manifests itself in flat momentum distributions for  $\theta \leq 24^\circ$  at the smaller momentum region. There, the momentum distributions decrease with angle only in a slow manner, much slower than what one obtains for a Gaussian distribution. The nonisotropy can only be obtained by allowing different widths in the longitudinal and transverse directions. Accordingly, we analyze the central collision component in terms of a "Fermi-Dirac" momentum distribution given by<sup>18</sup>

$$F_C(\vec{p}_{\text{lab}}) = A_C \left[ 1 + \exp \left[ \frac{p_{CZ}^2}{2\sigma_{CZ}^2} + \frac{p_T^2}{2\sigma_{CT}^2} - \frac{\alpha^2}{2} \right] \right]^{-1}, \quad (8)$$

where the widths  $\sigma_{CZ}$  and  $\sigma_{CT}$  are allowed to vary independently. The fragmentation component is taken to be a Gaussian distribution of the form

$$F_F(\vec{p}_{\text{lab}}) = A_F \exp \left[ -\frac{p_{FZ}^2}{2\sigma_{FZ}^2} - \frac{p_T^2}{2\sigma_{FT}^2} \right]. \quad (9)$$

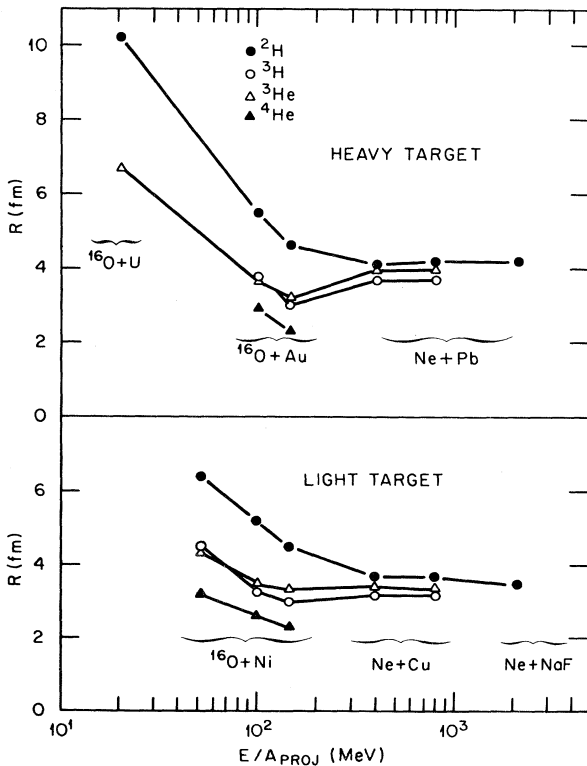


FIG. 13. Coalescence model radius parameters from composite light ions from <sup>16</sup>O and Ne induced reactions. Values obtained for the present data are compared with those from 20 MeV/nucleon <sup>16</sup>O + U data of Ref. 15 and 400–2100 MeV/nucleon Ne on Cu and Pb from Ref. 7.

TABLE VII. Parameters obtained by fitting light ion inclusive spectra with a two component model having independent longitudinal and transverse momentum widths as described in the text. Integral cross sections for the central ( $\sigma_C$ ) and fragmentation ( $\sigma_F$ ) contributions are also given.

$E/A_{\text{proj}}$	Target	$A_C$	$\sigma_{CZ}$	$\sigma_{CT}$	$\alpha$	$v_C/v_{\text{proj}}$	$\sigma_C$ (b)	$A_F$	$\sigma_{FZ}$	$\sigma_{FT}$	$v_F/v_{\text{proj}}$	$\sigma_F$ (b)
Protons												
51.8	Ni	0.065	100	106	1.8	0.49	2.69	0.29	73	76	1.0	2.09
100	Al	0.069	145	125	1.1	0.54	2.98	0.25	69	64	1.0	1.15
	Ni	0.092	147	128	1.1	0.52	4.25	0.32	69	65	1.0	1.56
	Sn	0.080	133	125	1.8	0.50	6.13	0.30	75	70	1.0	1.82
	Au	0.100	140	126	1.7	0.47	7.56	0.32	74	73	1.0	2.08
147	Ni	0.088	168	142	0.97	0.54	5.23	0.44	64	60	1.0	1.66
	Au	0.109	164	148	1.1	0.49	7.36	0.43	70	70	1.0	2.41
Deuterons												
51.8	Ni	0.039	182	151	1.2	0.49	1.68	0.058	103	112	1.0	0.62
100	Al	0.024	242	189	0.5	0.58	1.45	0.076	111	99	1.0	0.69
	Ni	0.036	242	190	0.3	0.53	2.05	0.070	119	112	1.0	0.89
	Sn	0.039	240	188	1.1	0.49	3.36	0.107	119	105	1.0	1.16
	Au	0.056	244	194	0.77	0.50	4.02	0.097	117	114	1.0	1.22
147	Ni	0.018	272	215	0.98	0.50	2.02	0.073	107	113	0.86	0.83
	Au	0.045	263	193	0.3	0.43	2.86	0.120	119	106	0.88	1.32
$^3\text{He}$												
51.8	Ni	0.0046	254	225	0.26	0.59	0.26	0.022	144	147	0.96	0.38
100	Ni	0.0065	244	245	0.06	0.65	0.40	0.030	128	133	0.98	0.39
147	Ni	0.0013	256	246	2.1	0.60	0.35	0.028	141	145	0.92	0.46
Alphas												
51.8	Ni	0.035	259	225	0.57	0.62	1.66	0.11	134	154	0.96	1.45
100	Al	0.0086	260	240	0.23	0.71	0.42	0.12	131	135	0.95	1.23
	Ni	0.011	266	256	0.47	0.65	0.66	0.11	134	147	0.95	1.30
	Sn	0.014	262	249	0.04	0.70	0.72	0.094	142	157	0.95	1.39
	Au	0.016	263	253	0.39	0.67	0.88	0.11	139	156	0.95	1.51
147	Ni	0.0023	279	251	1.5	0.68	0.30	0.091	151	148	0.92	1.26
	Au	0.0023	304	243	1.9	0.67	0.45	0.16	115	143	0.93	1.62

These “sources” are assumed to move along the beam direction with velocities  $\beta_C$  and  $\beta_F$ , respectively. Thus, the longitudinal and transverse momenta in the source rest frames are related to the laboratory momentum,  $\vec{p}_{\text{lab}}$ , by the Lorentz transformation, e.g.,

$$p_{FL} = \gamma_F(p_{\text{lab}} \cos \theta - \beta_F E)$$

and  $p_T = p_{\text{lab}} \sin \theta$ . The least squares method was used to simultaneously fit the spectra from  $6^\circ$  to  $115^\circ$  for various projectile-target-ejectile combinations, and the resulting parameters are listed in Table VII. The  $^3\text{H}$  spectra were not analyzed since the particle energies exceeded the detector limits in many cases. Also, for  $^3\text{He}$  only the Ni target data were fitted since only the normalization factors  $A_C$  and  $A_F$  displayed a significant dependence on target mass. For the large angle spectra, one expects that there are substantial contributions from the target fragmentation process. A three component model, including target fragmentation, would be a reasonable model to use, but would introduce additional parameters beyond those in the two component model. In using the two component model to fit the data, we assign lesser weights to the data points in the backward angles.

The final values of the parameters were undoubtedly in-

fluenced by the choice of initial values used in the search and, in particular, the velocities of the two components determine their behavior to a large extent. Typical starting values were  $v_C/v_{\text{proj}} \simeq 0.5$  and  $v_F/v_{\text{proj}} = 1.0$ . It should be noted that the values of  $v_F/v_{\text{proj}}$  for deuterons at 147 MeV/nucleon may be in error since the energies of the particles in the fragmentation peak exceeded the upper limit of the detectors and, therefore, the high energy end of the spectra may be distorted.

Fits to the proton, deuteron,  $^3\text{He}$ , and alpha particle spectra from 100 MeV/nucleon  $^{16}\text{O} + \text{Ni}$  are shown by the solid curves in Figs. 14, 15, 16, and 17, respectively. The spectra of lighter particles can be fitted quite well over the entire range of the data; however, the  $^3\text{He}$  and alpha particle yields observed at  $\theta > 24^\circ$  are not reproduced. This discrepancy becomes more pronounced with increasing projectile energy and target mass and may indicate that target fragmentation is becoming more important in this range of bombarding energies.

The fragmentation widths,  $\sigma_{FZ}$  and  $\sigma_{FT}$ , are found to be relatively insensitive to either the target mass or the projectile energy, and for a given projectile-target combination  $\sigma_{FZ} \approx \sigma_{FT}$ . This is consistent with the conjecture that the fragmentation component involves small momen-

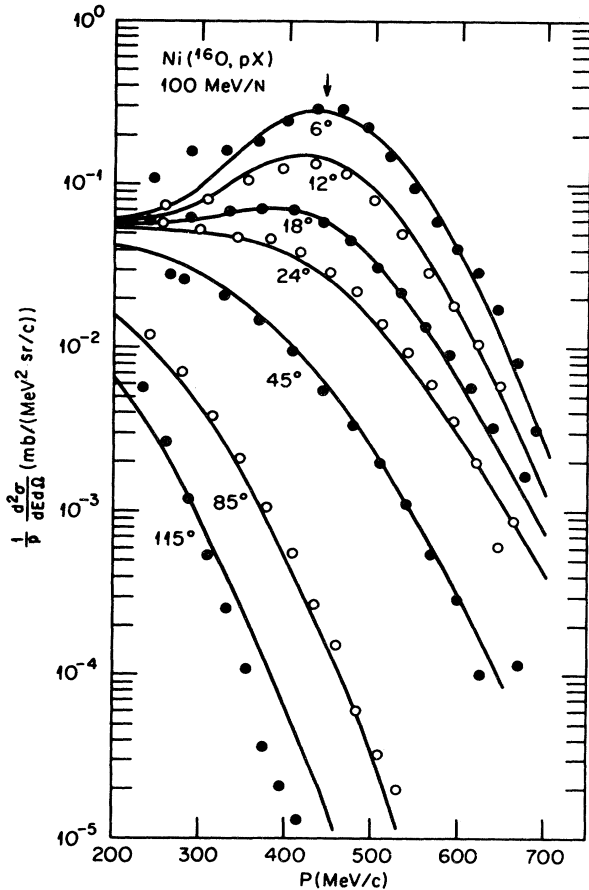


FIG. 14. Fits to proton spectra from  $^{16}\text{O} + \text{Ni}$  at 100 MeV/nucleon using a parameterization which includes both central and peripheral components as described in the text. The arrow indicates the momentum corresponding to the projectile velocity.

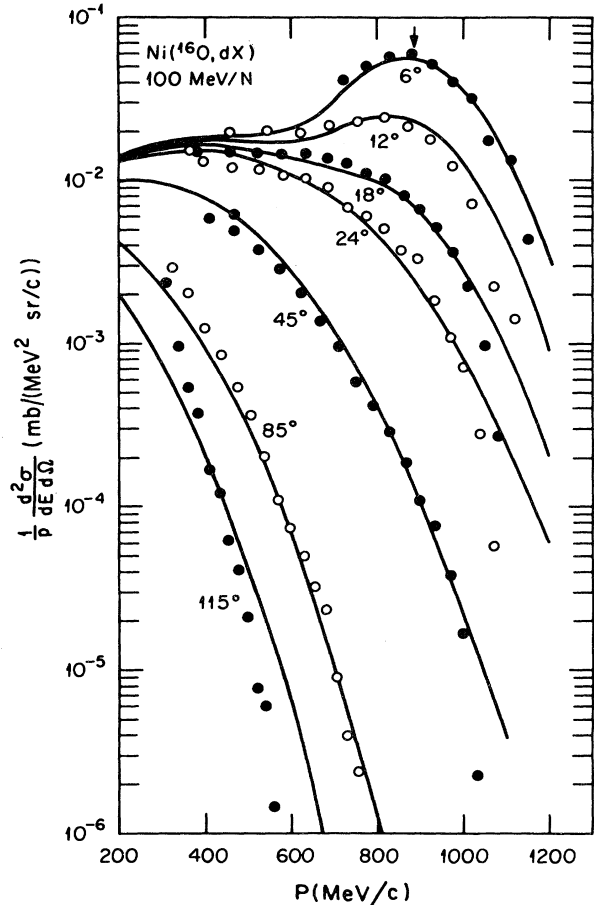


FIG. 15. Same as Fig. 14 but for deuterons.

tum transfers and is therefore described primarily by the momentum distribution of nucleons in the incident projectile. Using the expression given in Sec. III and averaging over values of  $\sigma_{FZ}$  and  $\sigma_{FT}$  for each particle, we obtain  $\sigma_0 = 69 \pm 5$  MeV/c for protons and  $\sigma_0 = 80 \pm 5$  MeV/c for  $A=2-4$ . The latter value is in good agreement with that obtained in studies of heavier fragments.<sup>19,20</sup> It is not clear whether or not the smaller value obtained for protons is significant, but it could indicate that the fragmentation process leading to nucleon emission is different from that for composite particles.

A closer examination of  $\sigma_{FZ}$  and  $\sigma_{FT}$  reveals several small but persistent trends in these parameters. For example, the values for protons show a systematic increase with increasing target mass or decreasing projectile energy. It is also interesting that  $\sigma_{FT} > \sigma_{FZ}$  for alpha particles. A similar result has been reported for heavier fragments and ascribed to an increase in the transverse width owing to orbital dispersion.<sup>19</sup> Another possible explanation is an unequal reduction of the widths. For example, substantial reductions from the independent particle values,  $\sigma_0^2 = p_F^2/5$ , were obtained by including Pauli correlations.<sup>21</sup> However, it is not yet known if these correlations would

produce the observed anisotropy in the momentum distribution.

The most obvious difference between the fragmentation and central collision parameters is the much larger momentum widths obtained for the central component. These values are typically twice those for the fragmentation component and, at least for protons and deuterons, the central collision widths are more sensitive to the projectile energy. As noted earlier, for thermal emission the widths can be related to the temperature of the source. Using the expression given in Sec. III, the values of  $\sigma_{CT}$  are found to give temperatures which, in most cases, are comparable to those extracted in the single moving source fits. This is reasonable since the latter were restricted to larger angles where the transverse width should be the controlling factor. However, there are appreciable anisotropies in the momentum distributions which can be interpreted as an indication that the central "source" is not an equilibrated system of nucleons. Thus the use of the relation between momentum width and temperature, and indeed the entire concept of "source temperature," is questionable. Finally, the non-Gaussian nature of the proton distributions is indicated by the presence of large values of  $\alpha$ . This "Fermi-Dirac" type of momentum distribution may have its origin in the initial momentum distributions

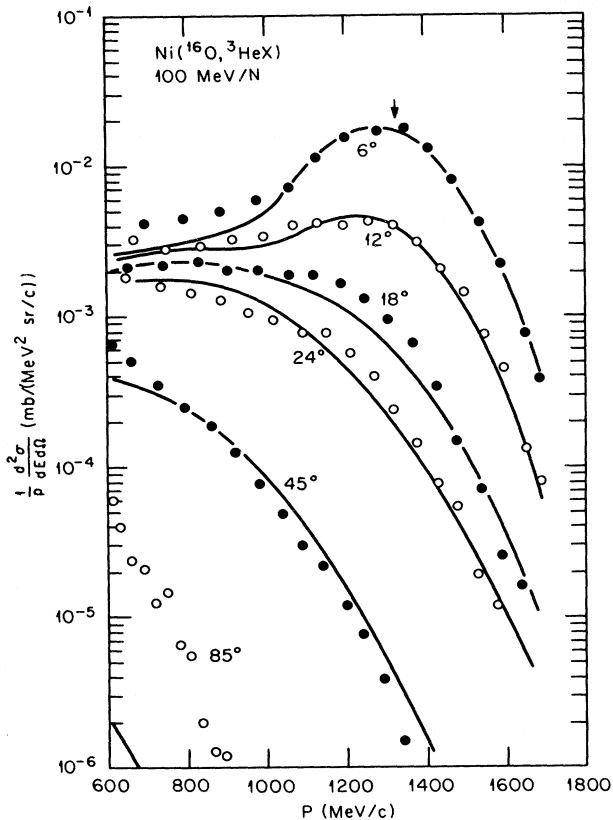


FIG. 16. Same as Fig. 13 but for  ${}^3\text{He}$ . The  $115^\circ$  data are off scale.

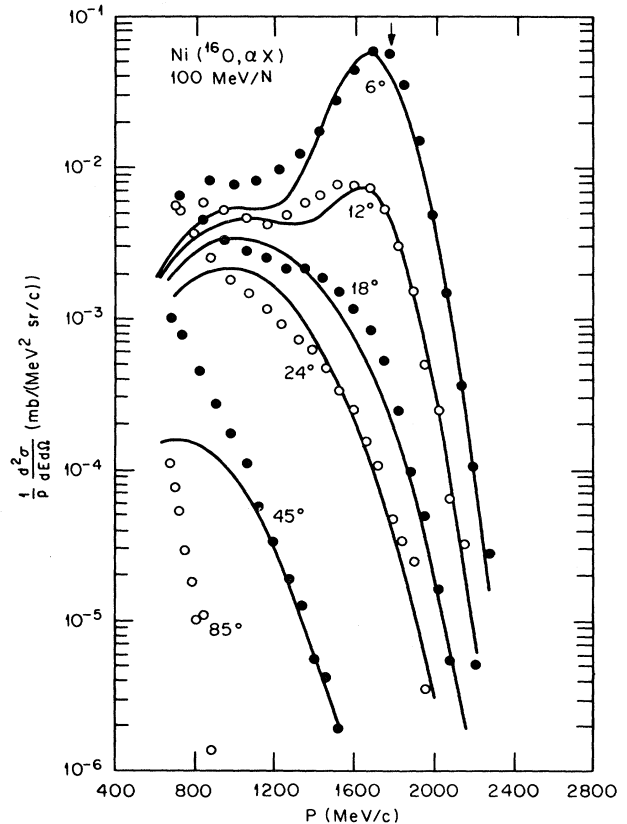


FIG. 17. Same as Fig. 14 but for alpha particles. The  $115^\circ$  data are off scale.

of nucleons of the two colliding nuclei.

Included in Table VII are integral cross sections for the central collision ( $\sigma_C$ ) are fragmentation ( $\sigma_F$ ) components obtained by integration of the fitted expressions. For protons and deuterons, their sums are in good agreement with the values obtained by extrapolation of the experimental data (Table IV), and in most cases the central term accounts for approximately 75% of the yield. The situation is quite different for alpha particles where, with the exception of the 51.8 MeV/nucleon data, the central component is much smaller than the fragmentation, and the sums account for only 36% (Au target) to 69% (Al target) of the measured yields. The agreement could probably be improved by increasing the weight of the large angle ( $\geq 45^\circ$ ) data, but at the expense of poorer fits at the smaller angles. As mentioned above, we prefer to attribute at least a part of this difference to the neglect of fragmentation of the excited target nuclei.

### V. SUMMARY

These studies have examined the influence of target mass and projectile energy on light ion ( $A \leq 4$ ) inclusive spectra at intermediate projectile energies (50–150 MeV/nucleon). At small angles large cross sections are measured for particles having velocities close to that of

the projectile. At these angles the cross sections are observed to have a relatively weak ( $\approx A^{1/3}$ ) dependence on the size of the target nucleus. As the emission angle increases, the spectra become more nearly exponential in shape and the cross sections display a greater sensitivity to the target mass ( $\approx A^{2/3}$ ). These characteristics suggest that the light ion emission process can be roughly divided into two major components, which are referred to as “peripheral fragmentation” and “central collisions.” For deuterons and tritons there are, in addition to the gross dependence on target mass, finer details which may indicate that target neutron contributions are important in the formation of these particles.

The projectile energy dependence is found to be quite different for the various particles. When the cross sections measured in these studies are compared with those reported at higher projectile energies it is found that while the proton yields increase dramatically with increasing projectile energy, composite particle yields either change very little ( ${}^2\text{H}, {}^3\text{H}, {}^3\text{He}$ ) or decrease rapidly ( ${}^4\text{He}$ ).

Three “models” were employed to analyze the data and to provide parameters which can serve as bases for comparisons with other measurements. A commonly used parametrization of light particle spectra involving emission from a heated, moving source was tried but, because of the dual character exhibited by the present data, only a

limited angular range could be fitted with a given set of parameters. However, reasonable fits were obtained by restricting the angular range to  $\theta \geq 24^\circ$  and the velocity and temperature parameters were compared with those reported at lower projectile energies. The smooth increase in temperature and the nearly constant source/projectile velocity ratio suggest there are no abrupt changes in the nature of the central collision part of the light ion emission process for projectile energies from 7.5 to 147 MeV/nucleon.

The coalescence model was applied to the composite particle spectra and the resulting radius parameters were compared with those reported at projectile energies of 20 and 400–2100 MeV/nucleon. The size of the interaction region is found to decrease as the projectile energy increases from 20 to about 200 MeV/nucleon and then to remain nearly constant, at a value comparable to the size of the projectile, at higher energies. In these studies, this model is found to have two major defects: overprediction of the fragmentation part of the spectra and underprediction of the low energy alpha particle yields.

In the third "model," it is assumed that the light ion emission process can be approximated by the sum of two contributions: peripheral fragmentation and central collisions. Each component is described by a momentum distribution having independent longitudinal and transverse

widths. This formulation provides good fits to the data for all but the alpha particles. The poor fits to the low energy part of the alpha particle spectra is tentatively attributed to the neglect of target fragmentation. The longitudinal and transverse widths obtained for the fragmentation component are nearly equal and suggest that the fragmentation process is governed primarily by the Fermi momentum of the projectile, although other effects may be indicated by the alpha particle data. The momentum distributions obtained for the central collision component are anisotropic and non-Gaussian, implying that thermal equilibrium is not achieved at the time of emission. Integration of the two components of the fitted curves provides an estimate of their relative contributions. For protons and deuterons, the central collision term accounts for about 75% of the integral cross section.

#### ACKNOWLEDGMENTS

We wish to thank the operating staff of the LBL Bevalac for their assistance and for providing high quality beams which allowed maximum utilization of the allotted beam time. This work was sponsored by the U. S. Department of Energy, under contract W-7405-eng-26 with the Union Carbide Corporation.

- 
- <sup>1</sup>J. B. Ball, C. B. Fulmer, M. L. Mallory, and R. L. Robinson, *Phys. Rev. Lett.* **40**, 1698 (1978).
- <sup>2</sup>C. B. Fulmer, J. B. Ball, R. L. Ferguson, R. L. Robinson, and J. R. Wu, *Phys. Lett.* **100B**, 305 (1981).
- <sup>3</sup>T. C. Awes, G. Poggi, S. Saini, C. K. Gelbke, R. Legrain, and G. D. Westfall, *Phys. Lett.* **103B**, 417 (1981).
- <sup>4</sup>T. J. M. Symons, P. Doll, M. Bini, D. L. Hendrie, J. Mahoney, G. Mantzouranis, D. K. Scott, K. Van Bibber, Y. P. Viyogi, H. H. Wieman, and C. K. Gelbke, *Phys. Lett.* **94B**, 131 (1980).
- <sup>5</sup>R. L. Auble, J. B. Ball, F. E. Bertrand, R. L. Ferguson, C. B. Fulmer, I. Y. Lee, R. L. Robinson, G. R. Young, J. R. Wu, J. C. Wells, and H. Yamada, *Phys. Rev. C* **25**, 2504 (1982).
- <sup>6</sup>A. Sandoval, H. H. Gutbrod, W. G. Meyer, R. Stock, Ch. Lukner, A. M. Poskanzer, J. Gosset, J. C. Jourdain, C. H. King, G. King, N. Van Sen, G. D. Westfall, and K. L. Wolf, *Phys. Rev. C* **21**, 1321 (1980).
- <sup>7</sup>S. Nagamiya, M. C. Lemaire, E. Moeller, S. Schnetzer, G. Shapiro, H. Steiner, and I. Tanihata, *Phys. Rev. C* **24**, 971 (1981).
- <sup>8</sup>B. Jakobsson, L. Carlén, P. Kristiansson, J. Krumlinde, A. Oskarsson, I. Otterlund, B. Schroder, H. A. Gustafsson, T. Johansson, H. Rhyde, G. Tibell, J. P. Bondorf, G. Fai, A. O. T. Karvinen, O. B. Nielsen, M. Buenerd, J. Cole, D. Lebrun, J. M. Loiseaux, P. Martin, R. Ost, P. deSaintignon, C. Guet, E. Monnard, J. Mougey, H. Nifenecker, P. Perrin, J. Pinston, C. Ristori, and F. Schussler, *Phys. Lett.* **102B**, 121 (1981).
- <sup>9</sup>J. B. Natowitz, M. N. Namboodiri, L. Adler, R. P. Schmitt, R. L. Watson, S. Simon, M. Berlinger, and R. Choudhury, *Phys. Rev. Lett.* **47**, 1114 (1981).
- <sup>10</sup>G. D. Westfall, B. V. Jacak, N. Anantaraman, M. V. Curtin, G. M. Crawley, C. K. Gelbke, B. Hasselquist, W. G. Lynch, D. K. Scott, B. M. Tsang, M. J. Murphy, T. J. M. Symons, R. Legrain, and T. J. Majors, Michigan State University Cyclotron Laboratory MSUCL-365, 1982.
- <sup>11</sup>H. H. Gutbrod, A. Sandoval, P. J. Johansen, A. M. Poskanzer, J. Gossett, W. G. Meyer, G. D. Westfall, and R. Stock, *Phys. Rev. Lett.* **37**, 667 (1976).
- <sup>12</sup>D. F. Measday and C. Richard-Serre, *Nucl. Instrum. Methods* **76**, 45 (1969).
- <sup>13</sup>A. S. Goldhaber, *Phys. Lett.* **53B**, 306 (1974).
- <sup>14</sup>R. L. Auble, J. B. Ball, F. E. Bertrand, C. B. Fulmer, D. C. Hensley, I. Y. Lee, R. L. Robinson, P. H. Stelson, D. L. Hendrie, H. D. Holmgren, J. D. Silk, and H. Breuer, *Phys. Rev. Lett.* **49**, 441 (1982).
- <sup>15</sup>T. C. Awes, C. K. Gelbke, G. Poggi, B. B. Back, B. Glagola, H. Breuer, V. E. Viola, Jr., and T. J. M. Symons, *Phys. Rev. Lett.* **45**, 513 (1980).
- <sup>16</sup>M.-C. Lemaire, S. Nagamiya, S. Schnetzer, H. Steiner, and I. Tanihata, *Phys. Lett.* **85B**, 38 (1979).
- <sup>17</sup>A. Mekjian, *Phys. Lett.* **89B**, 177 (1980), and references therein.
- <sup>18</sup>C. Y. Wong, Proceedings of the Fifth Heavy Ion Study, 1981, Lawrence Berkeley Laboratory Report LBL-12662, p. 61.
- <sup>19</sup>K. Van Bibber, D. L. Hendrie, D. K. Scott, H. H. Weiman, L. S. Schroeder, J. V. Geaga, S. A. Cessin, R. Treuhaft, Y. J. Grossiord, J. O. Rasmussen, and C. Y. Wong, *Phys. Rev. Lett.* **43**, 840 (1979).
- <sup>20</sup>Cheuk-Yin Wong and K. Van Bibber, *Phys. Rev. C* **25**, 2990 (1982).
- <sup>21</sup>G. Bertsch, *Phys. Rev. Lett.* **46**, 472 (1981).